Sensitivities and Mechanisms of the Zonal Mean Atmospheric Circulation Response to Tropical Warming

LANTAO SUN

Department of Earth and Atmospheric Sciences, Cornell University, Ithaca, New York, and National Center for Atmospheric Research, Boulder, Colorado

GANG CHEN

Department of Earth and Atmospheric Sciences, Cornell University, Ithaca, New York

JIAN LU

COLA/Department of Atmospheric, Oceanic and Earth Sciences, George Mason University, Fairfax, Virginia

ABSTRACT

Although El Niño and global warming are both characterized by warming in the tropical upper troposphere, the latitudinal changes of the Hadley cell edge and midlatitude eddy-driven jet are opposite in sign. Using an idealized dry atmospheric model, the zonal mean circulation changes are investigated with respect to different patterns of tropical warming. Generally speaking, an equatorward shift in circulation takes place in the presence of enhanced tropical temperature gradient or narrow tropical warming, similar to the changes associated with El Niño events. In contrast, the zonal mean atmospheric circulations expand or shift poleward in response to upper-tropospheric warming or broad tropical warming, resembling the changes under future global warming.

The mechanisms underlying these opposite changes in circulation are investigated by comparing the dry dynamical responses to a narrow tropical warming and a broad warming as analogs for El Niño and global warming. When running the idealized model in a zonally symmetric configuration in which the eddy feedback is disabled, both the narrow and broad warmings give rise to an equatorward shift of the subtropical jet. The eddy adjustment is further examined using large ensembles of transient response to a sudden switch-on of the forcing. For both narrow and broad tropical warmings, the jets move equatorward initially. In the subsequent adjustment, the initial equatorward shift is further enhanced and sustained by the low-level baroclinicity under the narrow tropical warming, whereas the initial equatorward shift transitions to a poleward shift associated with altered irreversible mixing of potential vorticity in the upper troposphere in the case of broad warming.

1. Introduction

It is well known that tropical heating can affect global atmospheric circulation and climate. During the warm phase of the El Niño–Southern Oscillation (ENSO), the enhanced tropical convection over the equatorial eastern Pacific cannot only excite a zonally asymmetric Rossby wave teleconnection pattern (e.g., Hoskins and Karoly 1981), it can also alter the tropical Hadley cell circulations and midlatitude zonal jets (Robinson 2002; Seager et al. 2003; L'Heureux and Thompson 2006; Lu et al. 2008;

Chen et al. 2008; Gong et al. 2010). The mechanisms for the contraction of the Hadley cell and the equatorward displacement of the midlatitude jet in response to the enhanced tropical heating during El Niño have been extensively studied and relatively well understood. Using an idealized atmospheric model, Chang (1995) investigated the effect of the Hadley circulation intensity on the extratropical winds by enhancing the meridional gradient of the tropical heating and found an equatorward shift of the jet stream associated with a stronger Hadley circulation, similar to the changes observed during El Niño. This extratropical response to the El Niño–like tropical heating can be understood as the impact of subtropical zonal wind anomalies on the equatorward propagation and absorption of the midlatitude eddies near their critical latitudes,

Corresponding author address: Lantao Sun, NCAR/CGD/CAS, P.O. Box 3000, Boulder, CO 80307-3000.
E-mail: lantao@ucar.edu

and subsequently on the eddy-driven extratropical circulation (e.g., Chang 1998; Robinson 2002; Seager et al. 2003; Chen et al. 2008). Additionally, the anomalous subtropical winds can affect the type or frequency of nonlinear wave breaking in the subtropics and thus shift the eddy-driven wind (e.g., Orlanski 2003; Gong et al. 2010). These studies suggest that if the thermally forced subtropical zonal wind is enhanced, then the extratropical eddy-driven wind would shift equatorward by the changes in either quasi-linear wave propagation or nonlinear wave breaking.

The enhanced equatorial SST warming (Liu et al. 2005; Vecchi et al. 2008; Collins et al. 2010; Lu and Zhao 2012) under increased greenhouse gases (GHGs) is also expected to give rise to a stronger subtropical jet by a thermal wind relationship. As demonstrated in Lu et al. (2008) and Chen et al. (2008), both El Niño and GHG forcings can give rise to an enhancement of the subtropical wind on the jet's equatorial flank. More recently, by forcing an aqua-planet atmospheric model with an abrupt switch-on of a 4-K uniform SST warming, the initial phase of the ensemble adjustment is characterized by an intensification of the Hadley cell and subtropical zonal wind (Chen et al. 2013), a pattern resembling that forced by the enhanced gradient of the tropical heating in Chang (1995). The similar subtropical wind response between El Niño and global warming is rooted in the fundamental Hadley circulation dynamics: the small Coriolis parameter near the equator and the nearly angular-momentum conserving tropical wind cannot sustain a large-scale temperature gradient and the effect of the tropical heating can spread over the entire tropics, thus constraining the anomalous temperature gradient and associated thermal wind near the edge of the tropics (e.g., Held and Hou 1980; Bretherton and Sobel 2003). If the same eddy adjustment as observed during El Niño were operating in isolation, the enhanced equatorial SST warming and associated subtropical wind under climate warming should have given rise to a similar equatorward shift in circulation. Taken at face value, it seems paradoxical that, under climate warming scenarios, the Coupled Model Intercomparison Project phase 3 (CMIP3) models tend to simulate a poleward expansion of the Hadley cell (Lu et al. 2007, 2008) and a poleward shift of the midlatitude storm tracks in both hemispheres (e.g., Yin 2005; Lorenz and DeWeaver 2007).

To further complicate the matter, in studying the sensitivities of the circulation change to the tropical heating in a dry atmospheric model, Butler et al. (2010) found no equatorward shift of the jet stream or contraction of the Hadley cell in response to tropical heating prescribed in the upper troposphere, even when the tropical heating is confined in the deep tropics. This seems to be contradictory to other idealized studies with dry (e.g., Chang 1995; Robinson 2002; Son

and Lee 2005) or moist models (e.g., Chen et al. 2010). We suspect that these apparent discrepancies are the results of the sensitivity of the circulation response to both the horizontal and vertical structures of the tropical heating. Therefore, using a dry dynamical model similar to previous idealized studies, we first explore the sensitivities of circulation with respect to the tropical temperature gradient as in Chang (1995) and the width of the tropical upper-tropospheric warming as in Butler et al. (2010). We find results consistent with the previous studies and the aforementioned sensitivities can be reconciled within a single dynamical model. Further, we identify an intriguing set of experiments in which an equatorward-to-poleward transition in circulation occurs as the meridional extent of tropical heating is broadened. This set of experiments is believed to hold the key to understanding the distinct mechanisms between the equatorward "El Niño–like" response versus the "global warming–like" poleward response to tropical heating.

The challenge of understanding the effect of the tropical heating arises from the intricate interplay between the thermally forced component of the circulation and the eddy adjustment to it. To isolate the effect of the eddy adjustment, we make use of the zonally symmetric version of our model to achieve the thermally forced response without the effect of the eddy feedbacks. Through this approach, we demonstrate that the eddy feedbacks are indispensable in the equilibrium solution as the zonal mean circulation undergoes an equatorward-to-poleward transition with gradually widened tropical warming. To further diagnose the eddy adjustment processes, a finite-amplitude wave activity budget is developed following Nakamura and Zhu (2010) and Nakamura and Solomon (2010). This hybrid Eulerian–Lagrangian formalism of the wave activity budget overcomes the difficulty of defining the wave activity in the regions of vanishing potential vorticity (PV) gradient. Since this diagnostic framework applies to both small-amplitude and finite-amplitude eddies, it aids in revealing the effect of the irreversible processes on the zonal jets, which are crucial for discerning the distinct mechanisms between the equatorward and poleward circulation shifts.

The paper is structured as follows. In section 2, we will briefly describe the dry atmospheric model, its zonally symmetric version, and the thermal forcings used for the perturbation experiments. The equilibrium responses to three sets of thermal perturbations will be discussed in section 3. The results of the large-size ensemble transient experiments will be presented and discussed in section 4. A novel diagnostic using the framework of finite-amplitude wave activity budget will be performed in section 5 to probe into the mechanisms of the eddy feedback during the transient response to tropical warming. The paper will conclude with discussion and conclusions.

2. Model description and experiment setup

a. Full model and thermal perturbations

We use the Geophysical Fluid Dynamics Laboratory (GFDL) atmospheric dynamical core with the Held and Suarez (1994) forcing. More specifically, the model is forced by a relaxation toward a prescribed zonally symmetric radiative-equilibrium-temperature profile and damped by a linear friction in the planetary boundary layer. In the control simulation, the radiative equilibrium temperature is specified as

$$T_{eq}^c(\phi, p) = \max\left\{200\,\text{K}, \left[315\,\text{K} - \boxed{\delta_y \sin^2\phi} - \delta_z \log\left(\frac{p}{p_0}\right)\cos^2\phi\right] \times \left(\frac{p}{p_0}\right)^\kappa\right\}, \tag{1}$$

where $\delta_y = 60\,\text{K}$, $\delta_z = 10\,\text{K}$. The integrations are performed at the spectral resolution of rhomboidal 30 spherical harmonic truncations (R30) with 20 evenly spaced sigma levels in the vertical. Eighth-order horizontal diffusion is used throughout the domain with the strongest damping at a time scale of 0.1 day for the smallest horizontal scales resolved in the model. In addition, to test the robustness of our results, we also run the model with three more settings: 1) rhomboidal 60 spherical harmonic truncations (R60), 2) vertical 30 uneven sigma levels (L30) the same as Scinocca and Haynes (1998), and 3) sixth-order horizontal diffusion, respectively.

In the perturbation experiments, diabatic heating is introduced by modifying the equilibrium temperature in the tropical troposphere. The change in the radiative equilibrium temperature multiplied by the thermal damping rate yields the perturbation in diabatic heating rate. Three sets of thermal perturbations are examined by adding different perturbations to the box in Eq. (1), so that

$$T_{eq}^p(\phi, p) = \max\left(200\,\text{K}, \left\{315\,\text{K} - \boxed{\delta_y[\sin^2\phi + \mathcal{F}(\phi,p)\mathcal{W}(\phi,\phi_0)]} - \delta_z \log\left(\frac{p}{p_0}\right)\cos^2\phi\right\} \times \left(\frac{p}{p_0}\right)^\kappa\right), \tag{2}$$

where $\mathcal{F}(\phi, p)$ is the thermal perturbation and $\mathcal{W}(\phi, \phi_0) = 0.5\{1 - \tanh[(|\phi| - \phi_0)/\delta\phi]\}$ is a weighting function to specify the meridional structure of thermal perturbations, with ϕ_0 setting the boundary of the thermal perturbation and $\delta\phi = 5°$ controlling the sharpness of the boundary. Within each set of experiment, we test the sensitivities of the equilibrium solution to different widths of the heating by varying ϕ_0 from $10°$ to $30°$ with an increment of $5°$. The formulations are summarized as follows, and the parameters for the three sets of thermal perturbations are listed in Table 1.

- *Tropical temperature gradient (TTG):* To mimic the configuration in Chang (1995), the meridional gradient of diabatic heating profile is enhanced in the deep tropics, by using

$$\mathcal{F}(\phi, p) = A + \sin^{1.25}(|\phi|) - \sin^2(\phi). \tag{3}$$

The constant A is included in the formulation to keep the global mean equilibrium temperature unchanged. As a result, this configuration leads to warming at the equator and cooling away from the equator (Fig. 1a).

- *Tropical upper-tropospheric warming (TUW):* Approximately following the heating profiles used in Butler et al. (2010), a tropical heating centered at the upper troposphere is added by using

$$\mathcal{F}(\phi, p) = A \times \exp\left[-\frac{(p/p_s - 0.3)^2}{2 \times 0.11^2}\right], \tag{4}$$

where A denotes the magnitude of the warming, and $\exp[-(p/p_s - 0.3)^2/(2 \times 0.11^2)]$ controls the vertical extents of the upper-tropospheric warming. Figure 1e shows the equilibrium temperature anomaly for this warming configuration.

- *Tropical tropospheric warming (TTW):* As in the TUW, but the equilibrium potential temperature change is independent of height within the troposphere,

$$\mathcal{F}(\phi, p) = A. \tag{5}$$

[Figures 3a and 3e show the equilibrium temperature anomaly for this configuration, with different width (ϕ_0).] Here $A = -0.1438$ is the same as in the TUW. When the width of the heating ϕ_0 is $10°$, this value corresponds to a global mean 1.5-K temperature increase at the surface. As shown later in this paper, the zonal mean midlatitude wind response to the narrow warming in this configuration is similar to that of TTG, while the response to the broad warming resembles that of TUW.

TABLE 1. The descriptions and parameters for the three sets of thermal perturbations. Equation (2) gives the radiative equilibrium temperature, where $\delta_y = 60$ K, $\delta_z = 10$ K. $\mathcal{F}(\phi, p)\mathcal{W}(\phi, \phi_0)$ determines the thermal forcing. For the TTG case, A varies with different width so that the global mean temperature is unchanged. For the other two warming cases, A is constant independent of the width of the warmings. $\mathcal{W}(\phi, \phi_0) = 0.5(1 - \tanh[(|\phi| - \phi_0)/\delta_\phi])$ and $\exp[(p/p_s - 0.3)^2/(2 \times 0.11^2)]$ are the meridional and vertical constraints for the thermal forcings, respectively. The transition latitude ϕ_0 determines the width of the thermal perturbation. See the text in section 2a for details.

Experiment and description	A	ϕ_0
Tropical temperature gradient (TTG): heating in	−0.0471	10°
the deep tropics and cooling in the subtropics;	−0.0637	15°
global mean temperature is unchanged.	−0.0793	20°
$\mathcal{F}(\phi, p) = A + \sin^{1.25}(|\phi|) - \sin^2(\phi)$	−0.0927	25°
	−0.1037	30°
Tropical upper-tropospheric warming (TUW):	−0.1438	10°
tropical heating distributed in the	−0.1438	15°
upper troposphere. $\mathcal{F}(\phi, p) = A \times$	−0.1438	20°
$\exp[(p/p_s - 0.3)^2/(2 \times 0.11^2)]$	−0.1438	25°
	−0.1438	30°
Tropical tropospheric warming (TTW): vertically	−0.1438	10°
uniform potential temperature perturbation	−0.1438	15°
in the troposphere. $\mathcal{F}(\phi, p) = A$	−0.1438	20°
	−0.1438	25°
	−0.1438	30°

b. Zonally symmetric model

The response to the prescribed thermal forcing without eddy feedbacks is obtained by making use of the zonally symmetric version of the model. In the zonally symmetric configuration, only the zonal mean part (spectral zonal wavenumber 0) is integrated forward in time. The contributions from eddies in the full model are added as external forcing to the primitive equations, so that the zonally symmetric model yields the same time-mean circulation as does the full model. The details for this type of zonally symmetric model can be found in Kushner and Polvani (2004).

c. Equilibrium and transient runs

The atmospheric responses to tropical warming are investigated using both equilibrium and transient simulations. In the equilibrated experiments, we run each case for 4000 days, at which point the model has established a statistical equilibrium. For the selected thermal forcing of interest, we also run 100-member ensembles of transient experiments with a sudden switch-on of forcing. These transient experiments can help to explain how the circulation evolves gradually from the control climate to the perturbed climate. To this end, we first run the control experiment for 7000 days, of which from every fiftieth day of the last 5000 days, 100 realizations branch out to generate an ensemble. For each of the 100 realizations, the thermal perturbation is switched on instantaneously, and the model integrates for 200 days toward a new equilibrium. Additionally, the equilibrium and transient experiments are performed in the zonally symmetric model for the same sets of thermal perturbations. As the zonally symmetric model consists of no eddies, a 1000-day integration is long enough to reach equilibrium. Only one realization of transient experiment is needed for the zonally symmetric model to capture the temporal response to external thermal forcings.

3. Equilibrium responses

In this section, we will show that all the results reviewed in introduction can be reconciled in a single modeling framework. We first show a TTG ($\phi_0 = 20°$) experiment similar to Chang (1995), that is, a heating within 10° latitude around the equator and cooling off the equator between 10° and 20° latitudes. Figures 1a–d respectively show the changes in equilibrium temperature and the circulation responses in overturning mass streamfunction, temperature, and zonal mean zonal wind. The enhanced diabatic heating gradient results in a strengthening and equatorward contraction of the Hadley cell. The temperature response is characterized by a weak uniform warming in the tropics, a cooling in the midlatitudes between 25° and 45°, and a warming farther poleward. The zonal wind response consists of a barotropic dipole straddling the core of the climatological jet so that the jet stream shifts equatorward as a result. All of the features described above are typical of the tropospheric response to El Niño (Seager et al. 2003; Lu et al. 2008) and in concert with the result of Chang (1995).

The TTG experiment is compared with a TUW ($\phi_0 = 30°$) experiment, similar to the configuration used in Butler et al. (2010), in Figs. 1e–h. In contrast to the TTG, the circulation response to TUW leads to a somewhat opposite picture in the midlatitudes. The Hadley cell weakens and expands poleward. The zonal wind also shifts poleward, in accordance with the poleward shift of the Ferrel cell. The temperature in this TUW experiment exhibits an opposite pattern to that in the TTG case (cf. Figs. 1g,c) except over the regions of the direct impact of the tropical forcing. These results again agree well with the similar case of Butler et al. (2010, see their Fig. 2).

To verify the robustness of the circulation shift in the TTG and TUW experiments, we further perform sensitivity experiments in which the edge of the tropical heating is systematically broadened from 10°N/S to 30°N/S with an increment of 5° (Fig. 2). As the boundary of the subtropical cooling in the TTG gradually extends
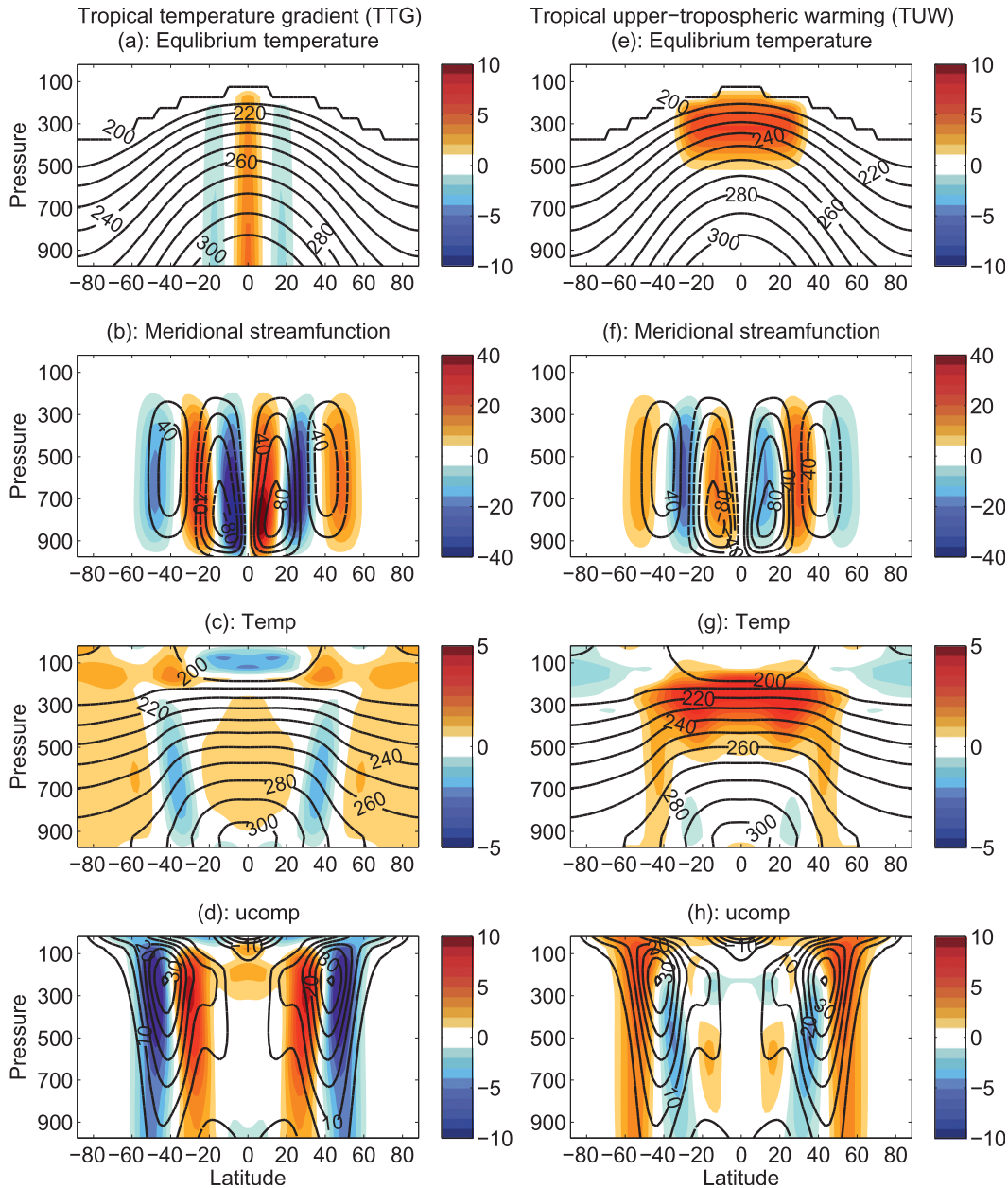
FIG. 1. Zonally averaged climatologies (contours) and equilibrated responses (shading) to (a)–(d) tropical temperature gradient ($\phi_0 = 20°$) and (e)–(h) tropical upper-tropospheric warming ($\phi_0 = 30°$) cases. (a),(e) Equilibrium temperature (K), (b),(f) meridional streamfunction ($10^9\,kg\,s^{-1}$), (c),(g) temperature (K), and (d),(h) zonal wind ($m\,s^{-1}$).

poleward, the TTG forcing tends to produce a greater shift in the jet. In the TTG group, although the westerly jet tends to shift equatorward with the intensity of the simulated Hadley cell, there is no simple linear proportionality between the two (Fig. 2b). Next, consistent with Butler et al. (2010), even the narrowest TUW forcing can produce a weak poleward shift of the eddy-driven jet (see Fig. 2a, triangles), while the shifts forced by the broader TUW forcings ($\geq 20°$) are much more pronounced.

Also, the TUW always weakens the Hadley cell, with a lower intensity accompanying a more poleward jet shift (Fig. 2b, triangles). In both sets of experiments examined, there is no change in the sign of the circulation shift. In summary, our modeling results agree with Chang (1995) and Butler et al. (2010): stronger tropical warming gradient generates a narrowed and strengthened Hadley cell and tropical upper-tropospheric warming results in a broadened and weakened Hadley cell.
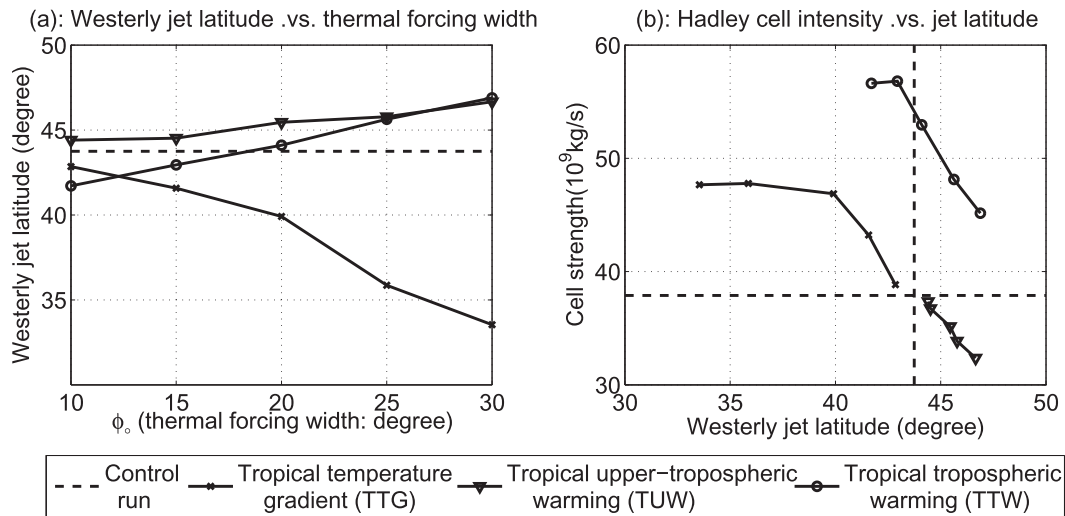
FIG. 2. (a) Equilibrated responses of westerly jet latitudes to the different width of the tropical thermal forcings. (b) Hadley cell intensity responses vs jet latitude responses for the equilibrated thermal forcing experiments. The intensity of the Hadley cell is measured by the maximum 500-hPa meridional streamfunction. The three types of tropical forcings are illustrated in Figs. 1 and 3.

Furthermore, when the tropical heating is prescribed throughout the troposphere with the TTW forcings, we see an equatorward-to-poleward transition as the breadth of the tropical heating is systematically expanded from 10°N/S to 30°N/S, with the transition point occurring around $\phi_0 = 17.5°$N/S (Fig. 2a). Interestingly, the circulation change with TTW exhibits a monotonic sensitivity to the meridional extent of the heating, with a broader heating driving a broader Hadley cell extent and a more poleward eddy-driven jet and a lower intensity of the Hadley cell (circles in Fig. 2). In contrast to the axisymmetric theory (Held and Hou 1980), the intensity of the Hadley cell is more sensitive to the heating gradient within the tropics than the equator-to-pole gradient; the extent of the Hadley cell does not have a simple proportional relationship with the equator-to-pole temperature gradient either.

Figure 3 illustrates the responses in circulation for narrow ($\phi_0 = 10°$, Figs. 3a–d) and broad ($\phi_0 = 30°$, Figs. 3e–h) TTW forcings. Both cases are characterized by a strengthening of the Hadley cell and a warming in the tropics. The extratropical responses, however, are distinct in both the latitudinal shifts of the westerly jet and the overturning circulation. The extratropical differences between the two cases resemble qualitatively those between the TTG and the TUW experiments in Fig. 1 or those between El Niño and global warming (Lu et al. 2008). Thus these two TTW experiments with differing tropical warming widths provide a pair of analogs in a dry dynamical framework corresponding to El Niño and global warming, respectively. In the following sections, the narrow versus broad TTW experiments will be analyzed in detail to probe into their underlying dynamics.

To test the sensitivities to the model settings, we also run the TTW experiments with different horizontal and vertical resolutions, and reduced order of hyperdiffusion (see section 2a for details). Figure 4 shows the latitudes of the westerly jet with different edges of the tropical heating for different model settings. When the tropical heating is broadened, all of the cases undergo a transition from the equatorward shift to the poleward shift of the jet. The magnitude of the zonal wind anomaly differs with model settings (not shown).

Can the distinct extratropical circulation changes between narrow and broad warmings be obtained merely through the zonally symmetric dynamics? We apply the same narrow versus broad TTW forcings as illustrated in the top panels in Fig. 3 to the zonally symmetric model, wherein the eddy forcing is fixed to be the same as in the control run and thus not allowed to respond to the thermal perturbation. Interestingly, both the narrow and broad TTW forcings drive characteristically similar patterns of tropical warming and produce an equatorward enhancement of the westerly jet (Fig. 5). This result pinpoints unequivocally the indispensable roles of the eddy feedbacks in producing the opposite equilibrated shifts of the westerly jet between the two cases. As both the zonal wind and PV gradient are altered on the climatological jet's equatorward flank, the conventional linear wave theory would predict an equatorward shift of the zonal jet for both cases through either wave refraction (Seager et al. 2003) or shift of the critical latitudes (Lu et al. 2008). Therefore, the small-amplitude linear theories are inadequate to explain the distinct full-model responses between the two cases, posing a challenge for us
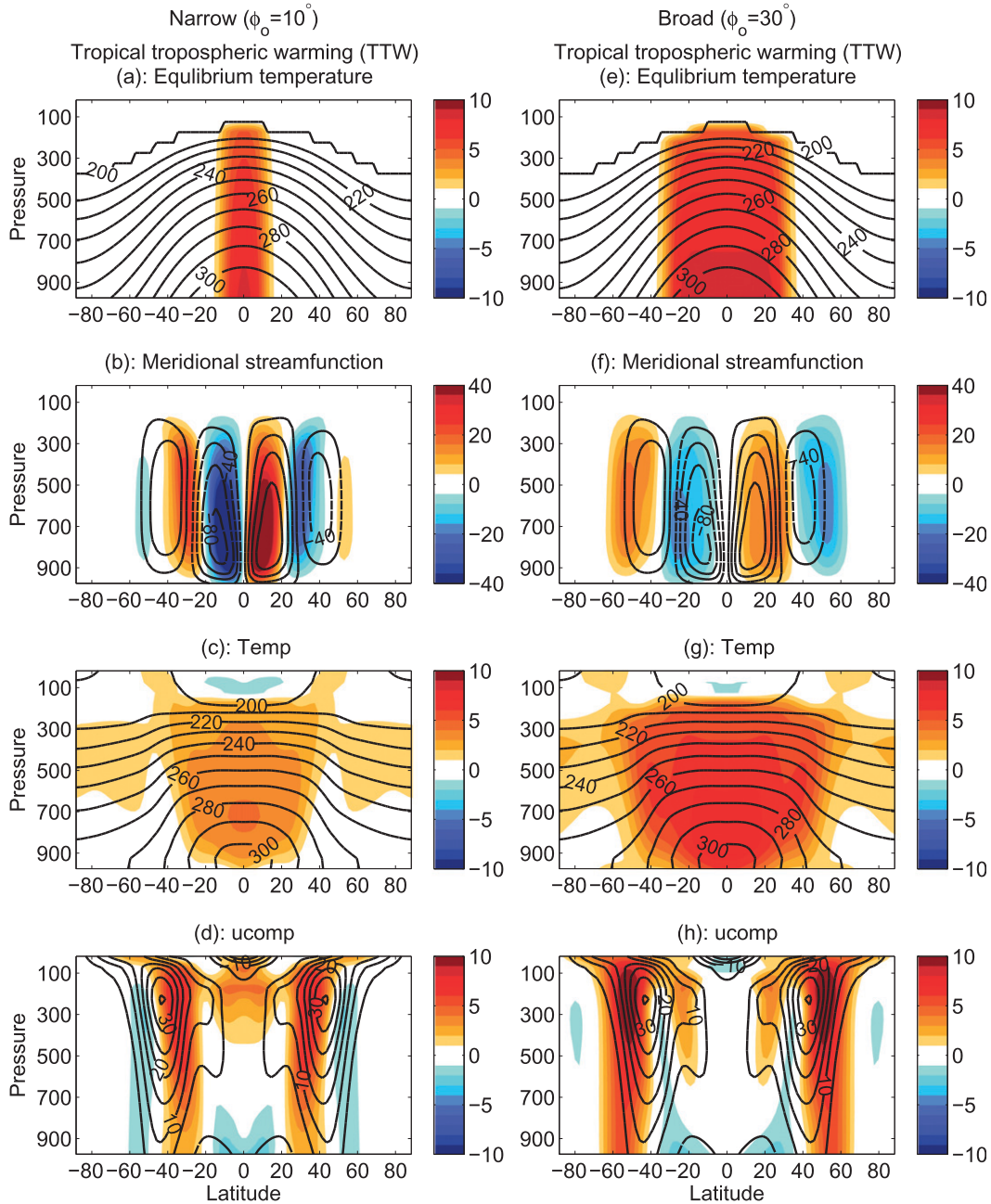
FIG. 3. Zonally averaged climatologies (contours) and equilibrated responses (shading) to the (a)–(d) narrow ($\phi_0 = 10°$) and (e)–(h) broad ($\phi_0 = 30°$) tropical tropospheric warming. (a),(e) Equilibrium temperature (K), (b),(f) meridional streamfunction (10^9 kg s^{-1}), (c),(g) temperature (K), and (d),(h) zonal wind (m s^{-1}).

to unravel the contrasting mechanisms between the El Niño–like and global warming–like circulation changes. This motivates us to perform large-size ensemble experiments with an abrupt switch-on of the thermal forcing for both cases and diagnose the day-to-day adjustment processes using a novel, finite-amplitude wave activity budget.

4. Transient responses to narrow versus broad tropical warming

To distinguish the mechanisms responsible for the opposite shift of the eddy-driven circulation between the narrow and the broad TTW cases, we resort to transient ensemble experiments, in which the thermal forcing is
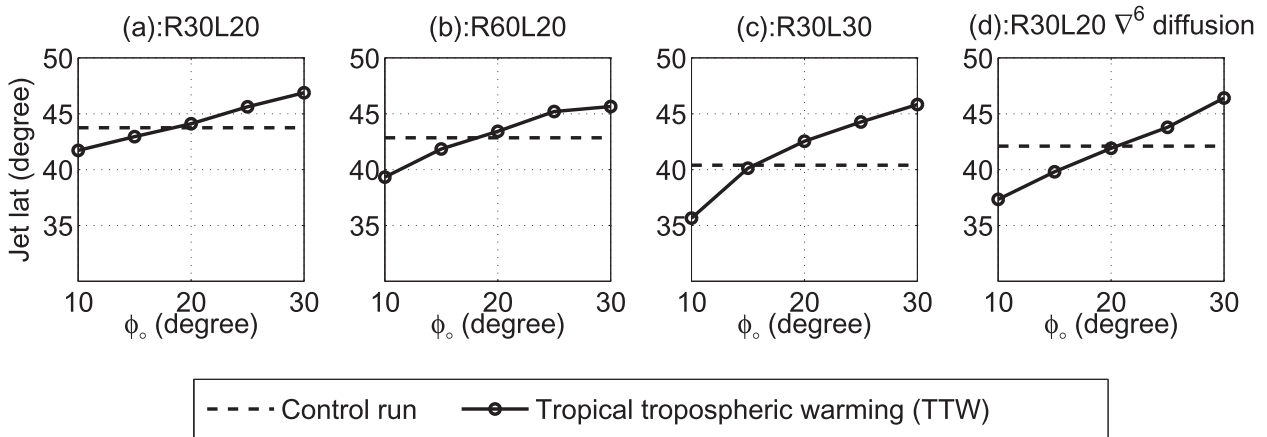
FIG. 4. Equilibrated responses of westerly jet latitudes to the different width of the tropical tropospheric warming for the different settings of the model. (a) Original horizontal R30 vertical 20 even-level setting. (b) As in (a), but for horizontal R60 resolution. (c) As in (a), but using the uneven 30 vertical levels as in Scinocca and Haynes (1998). (d) As in (a), but adopting a sixth-order diffusion scheme.

abruptly switched on and kept constant. The ensemble size is 100, but by averaging both hemispheres the actual sample size for the ensemble mean is 200. Note that even with the sample size of 200, the internal noise remains sizable in the ensemble mean, because of the vibrant internal variability of the midlatitude winds. The following investigation will be focused only on the forced ensemble-mean features.

The top panels of Fig. 6 show the evolutions of the anomalous zonal wind at 875 hPa in the transient experiments for the narrow (left) and broad (right) warmings

corresponding to the equilibrium solutions in Fig. 3. Initially for both cases, positive zonal wind anomalies appear between 20° and 40° latitude, indicating an equatorward enhancement or shift of the eddy-driven westerly jet. While the anomalies in the narrow warming case grow in intensity with little structural change and quickly reach equilibrium at around day 40, the positive anomalies in the broad warming case gradually shift poleward, undergoing a transition from an equatorward enhancement to a poleward shift. It takes more than 100 days for the ensemble-mean response to reach equilibrium.
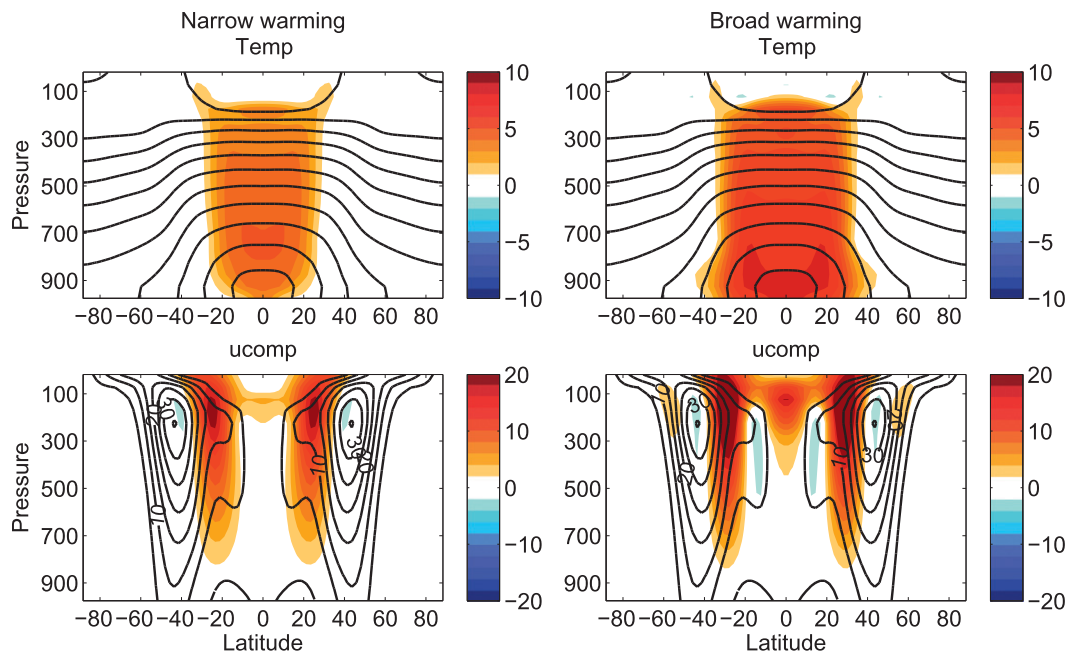

FIG. 5. Climatologies (contour) and equilibrated responses (shading) of temperature and zonal wind to (left) the narrow and (right) the broad tropical tropospheric warming in the zonally symmetric models, in which the same eddy forcings are derived from the control runs. The thermal perturbations are as in Fig. 3.
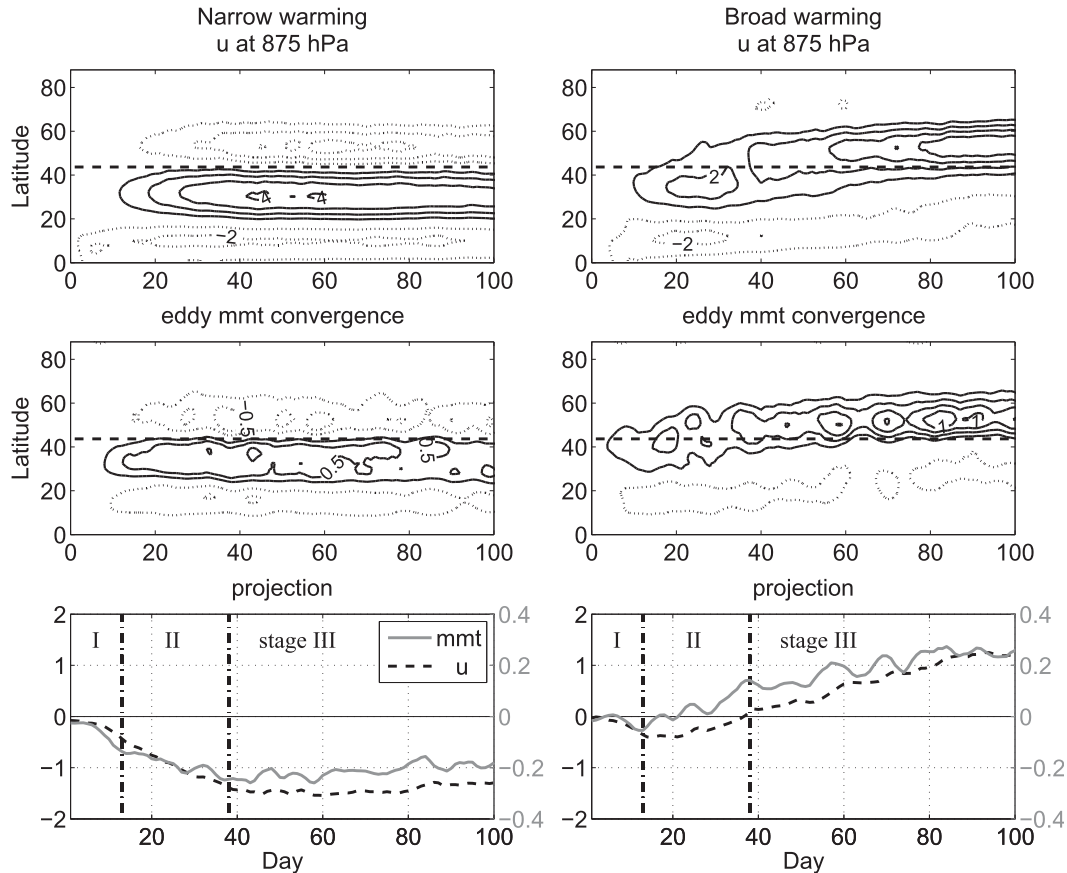
FIG. 6. (top) The evolutions of zonal mean zonal wind anomaly at 875 hPa in the transient experiments of (left) narrow and (right) broad warmings. (middle) As in (top), but for the vertically averaged eddy momentum convergence anomaly. The black-dashed lines in the top and middle panels denote the latitude of the climatological jet. (bottom) As in (top), but for the projection of the zonal wind and eddy momentum convergence onto the leading EOF of 875-hPa zonal wind. In the bottom panel, the left black dash-dotted line indicates day 13, in which the eddy momentum convergence projection minimizes in the broad warming; the right black dash-dotted line indicates day 38, in which the zonal wind projection transits from negative to positive in the broad warming.

The upper-tropospheric winds show similar evolutions but with larger magnitudes (not shown). We notice that the temporal evolution in the broad warming case is somewhat different from the similar ensemble transient simulation of Butler et al. (2011), wherein the zonal wind anomalies show little shift during the transient adjustment. This may be attributed to their small ensemble size (24 realizations), rendering the small initial changes hard to detect. The initial equatorward shifts we see in our model are also consistent with the thermally driven changes simulated in the zonally symmetric model.

Similar transient experiments are also performed using the zonally symmetric version of the model. Consistent with the equilibrated results in Fig. 5, the evolutions of the zonal winds for the narrow and broad warmings are similar, both characterized by a monotonic increase of the zonal wind in the subtropical upper troposphere. Thus, in

the absence of eddy feedback there is little change in the extratropics.

From the perspective of angular momentum balance, the midlatitude barotropic wind (with the time tendency term neglected) can be roughly thought of as the result of the balance between the eddy momentum convergence and the surface friction (e.g., Chen et al. 2007), which may be parameterized as a linear function of the near-surface zonal wind. Indeed, as shown in the middle panels of Fig. 6 the evolution of the vertically integrated eddy momentum convergence displays rather similar temporal structure to the near-surface wind. The dominance of the eddy momentum forcing is further confirmed by a direct calculation of the momentum advection by the zonal mean wind components: the latter in the extratropics is an order of magnitude smaller than the former, as expected from the quasigeostrophic scaling.

The lead–lag relationship between the phases of the eddy momentum forcing and the near-surface zonal wind is clearer when both are projected onto the pattern of the leading mode (i.e., the annular mode or zonal index) of the 875-hPa zonal wind (bottom panels of Fig. 6). On the one hand, for the narrow warming case, both projections show a monotonic acceleration with time toward the equilibrium state during the adjustment phase. No distinct phase lag or lead can be discerned between the eddy forcing and the 875-hPa zonal wind. On the other hand, for the broad warming case, consistent with the top-right panel of Fig. 6, the time series of the zonal index descends first (from day 1 to day 13) and then ascends afterward. As a result, the zonal index undergoes a negative-to-positive transition at approximately day 38. It is important to note that the transition of the eddy momentum forcing takes place much earlier and it is the positive projection of the eddy momentum forcing that is responsible for the upward swing of the zonal index between days 13 and 38.

In observing the similar tendencies of the evolutions between the narrow and broad warming cases during the first 13 days and the intriguing transition in the latter case, we divide the transient adjustments of the two ensemble experiments into three different stages: stage I (days 1–13) wherein the eddy-driven jet shifts equatorward in both warming cases; stage II (days 13–38) wherein the zonal index starts to turn around toward the transition point under broad warming, while it continues to grow in the same direction set by the initial stage under narrow warming; and stage III (day 38 onward) wherein the circulation is nearly in equilibrium for the narrow warming case, while the zonal index just crosses the transition point and starts ramping up toward a positive equilibrium. With the aid of this categorization, we may begin to address the issue with respect to the cause for the poleward shift of the westerly jet in the broad warming case.

5. Mechanisms of the tropospheric jet shift

The experiments and analyses above point unequivocally to the importance of the eddy adjustment in the poleward shift of the eddy-driven jet under broad tropical heating. Here, we strive to elucidate the mechanisms of eddy adjustment by the Eliassen–Palm (E–P) flux diagnostics, maximum Eady growth rate analysis, and a finite-amplitude wave activity budget.

a. E–P flux

Starting with the conventional transformed Eulerian-mean (TEM) momentum equation (Edmon et al. 1980; Andrews et al. 1987), we have

$$\frac{\partial \overline{u}}{\partial t} = f\overline{v}^* + \frac{1}{a\cos\phi}\mathbf{V}\cdot\mathbf{F} + \overline{X}, \quad (6)$$

where f is the Coriolis parameter, $\overline{v}^*$ is the residual meridional velocity, $\overline{X}$ is the friction near the surface, and $\mathbf{V}\cdot\mathbf{F}$ is the E–P divergence, which has the form

$$\frac{1}{a\cos\phi}\mathbf{V}\cdot\mathbf{F} = -\frac{1}{a\cos^2\phi}\frac{\partial(\overline{v'u'}\cos^2\phi)}{\partial\phi} + f\left(\frac{\overline{v'\theta'}}{\partial\Theta/\partial p}\right)_p, \quad (7)$$

where Θ is the global mean potential temperature θ at each pressure level. Assuming that eddies are geostrophic and ignoring the divergence associated with the gradient in f, it is readily shown that

$$\overline{v'q'} = \frac{1}{a\cos\phi}\mathbf{V}\cdot\mathbf{F}, \quad (8)$$

where the left-hand side is the zonal mean eddy PV flux, and q is the quasigeostrophic (QG) potential vorticity,

$$q = f + \zeta + f\frac{\partial}{\partial p}\left(\frac{\theta - \Theta}{\partial\Theta/\partial p}\right). \quad (9)$$

Figure 7a shows the climatological E–P flux (vectors) and divergence (shading), together with the momentum convergence (contours). The E–P vectors represent the propagation of the QG wave activity and are typically upward in midlatitude, veering equatorward aloft. The vertical component of the E–P flux arises from the meridional heat flux and acts to reduce the intensity of the midlatitude westerlies aloft, transferring angular momentum from the upper troposphere to the surface to be finally dissipated by the surface friction. The horizontal component of the E–P flux acts to extract angular momentum from the subtropics and deposit in the midlatitudes, so as to produce a westerly jet.

Under a sudden switch-on of the narrow tropical heating, the upward E–P flux is enhanced during stage I (from day 1 to day 13), giving rise to a convergence in the upper troposphere and a divergence in the lower troposphere (Fig. 7b). The anomalous upward E–P flux has a maximum at the equatorial flank of the climatological E–P flux maximum (and so the climatological jet), thus shifting equatorward the total distribution of the E–P flux and the momentum flux convergence/divergence. As such, the eddy-induced equatorward shift takes place immediately during the first phase of the transient adjustment. The adjustment of stage II (day 13–38) is characterized by a continuation of the enhancement of the upward wave activity propagation in the subtropics and a reduction poleward of it (Fig. 7c). The resultant
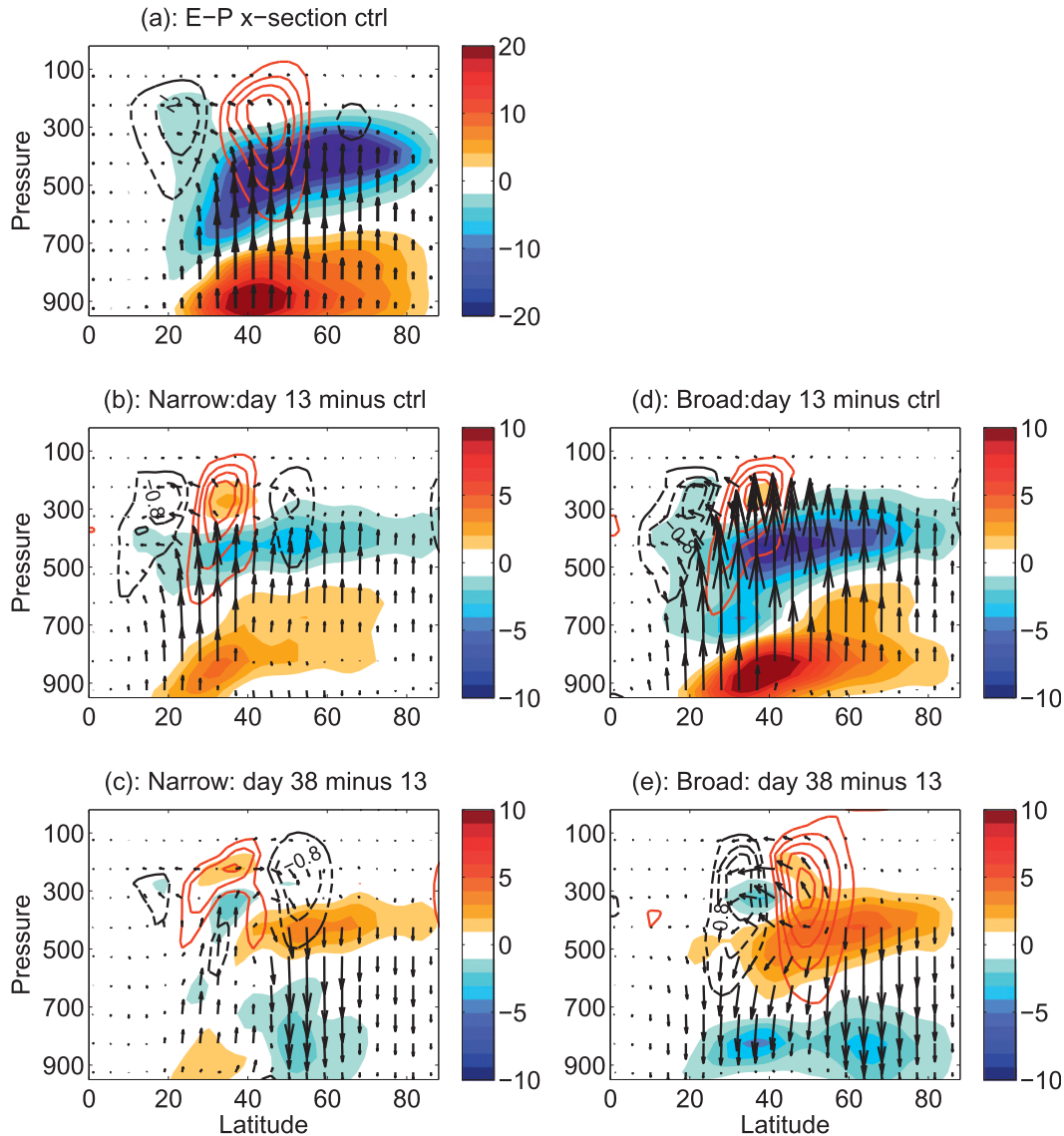
FIG. 7. (a) Climatological E–P vector (arrows), E–P flux divergence (shading), and eddy momentum convergence (contours) in the control experiments. The red solid contours denote the positive eddy momentum convergence and the black dashed contours denote the negative convergence. (b),(c) As in (a), but for the ensemble-mean anomalies of day 13, and changes from days 13 to 38 in the transient experiments under narrow warming. (d),(e) As in (a), but for the ensemble-mean anomalies of day 13, and changes from days 13 to 38 in the transient experiments with broad warming. The contour interval is $1 \, \mathrm{m \, s^{-1} \, day^{-1}}$ in (a) and $0.4 \, \mathrm{m \, s^{-1} \, day^{-1}}$ in (b)–(e).

momentum convergence/divergence reinforces the original structure resulted from stage I and drives the equatorward shift of the eddy-driven jet toward its equilibrium state. The tripolar structure of the eddy-induced momentum convergence/divergence is also consistent with the change diagnosed with the space–time cospectrum discussed in Chen et al. (2008), implicative of the involvement of the interaction between the enhanced subtropical wind and the equatorward propagation of the wave activity. Note, however, that a very similar

interaction also takes place during the first stage of the adjustment to the broad warming as well. We argue that it is the sustaining baroclinicity at the latitudes of 25°–30° imposed by the narrow tropical warming that provides the source of the wave activity and underpins the upper-level horizontal divergence of the wave activity flux. It is thus remarkable to see next for the broad warming case that the eddy momentum forcing begins to shift the jet poleward despite the fact that the lower-tropospheric baroclinicity remains at the equatorward side of the jet.

Figure 7d shows the changes of the E–P flux and momentum convergence during the first 13 days for the broad warming case. The adjustment during stage I bears a considerable resemblance to its counterpart of the narrow warming case: an overall enhancement of the upward wave activity flux, the upper-tropospheric convergence and lower-tropospheric divergence of the E–P flux. The magnitude for the broad warming case is larger and the impacts are more widely spread, thus projecting more strongly on the climatological flux and convergence. Interestingly, the corresponding anomalous momentum convergence is similar to the narrow warming case in both structure and magnitude and consequently exerts a similar negative projection onto the annular mode (cf. Fig. 6, bottom).

From day 13 to day 38 (stage II), the enhancement of the vertical E–P flux starts to attenuate (Fig. 7e). Different from the narrow warming (Fig. 7c), however, the attenuation of the vertical E–P flux spreads throughout the whole hemisphere instead of only in the extratropics. This seems to suggest that the enhancement of baroclinicity, initially located at the equatorward side of the westerly jet, is close to neutral. During this period, a large area of E–P divergence appears in the extratropical upper troposphere, acting as wave source to induce the wave to propagate downward and equatorward. Associated with this, there are momentum convergence in the extratropics and momentum divergence in the subtropics. Note that in the narrow warming, there is also such E–P divergence in the extratropics, but the magnitude is small and it has limited influence on the wave propagation in the upper troposphere.

One may suspect that the upper-level momentum convergence change during the stage II in the broad warming should be also attributed to the change of the lower-level baroclinicity as in the narrow warming cases. However, a closer inspection on the lower-tropospheric baroclinicity suggests the opposite, as to be elaborated in the next section.

b. Lower-tropospheric baroclinicity analysis

The lower-level baroclinicity can be measured by the maximum Eady growth rate (MEGR) (Lindzen and Farrell 1980):

$$\sigma = -\frac{0.31g}{N\Theta_0}\frac{1}{a}\frac{\partial\overline{\theta}}{\partial\phi}, \tag{10}$$

where g is the gravitational acceleration rate and N is Brunt–Väisälä frequency. Also, Θ_0 is the global mean potential temperature, and θ is the zonal mean potential temperature. The climatological MEGR in the troposphere peaks

at 42°N/S (not shown), consistent with the E–P diagnosis (Fig. 7a). Figures 8a and 8b show the evolution of the anomalous MEGR of the full model and zonally symmetric model adjustment, respectively, in the narrow warming case. In the former, the positive anomaly first appears near 20° in the subtropics but quickly weakens. In comparison with the time series of the annular mode projections (Fig. 6, bottom), the development of a positive (negative) MEGR anomaly at the equatorward (poleward) flank of the jet coincides with the growth of the negative projection of the eddy momentum forcing and the negative zonal index during the transient adjustment. The synchronous evolution of all the three renders a simple interpretation of the response in the narrow warming case as discussed above.

For the broad warming case, during the first stage (≤day 13) of the adjustment an anomalous baroclinicity first occurs at the equatorward flank of the jet, in concert with the eddy momentum acceleration at the similar latitudes associated with the equatorward enhancement of the E–P flux. The poleward shift of the momentum forcing during the second stage between day 13 and day 38, however, cannot be explained by the lower-level baroclinicity change, which remains at the equatorward side of the jet throughout this period. Furthermore, the projection of the eddy momentum forcing onto the annular mode tends to lead the projection of the baroclinicity (by comparing the right panels of Fig. 6 with Fig. 8c). Thus, one cannot use the baroclinicity argument to explain the rise of the momentum forcing for the jet shift in the broad warming case. Instead, as will be shown in the next section, it is the irreversible wave breaking in the upper troposphere that holds the key to understanding the origin of the poleward shift in momentum flux during stage II. During stage III, a poleward shift in the lower-level baroclinicity emerges and grows in intensity. Note that stage III is defined by the period when the eddy-driven jet is more poleward relative to the climatological jet. This suggests that as the jet starts to move poleward in stage III, this poleward shift is further reinforced by the changes in the lower-level baroclinicity, which provides a positive baroclinic feedback (e.g., Robinson 2000; Chen and Plumb 2009). A similar MEGR analysis is also performed for the corresponding adjustment in the zonally symmetric model. In the absence of eddy feedbacks, the zonally symmetric Hadley cell adjustment fixes the anomalous MEGR at 30° in the subtropics with little displacement throughout the evolution. The resultant MEGR anomalies are always located more equatorward relative to the full adjustment, highlighting the consequential role of eddies in shaping the thermal structure of the midlatitude atmosphere.
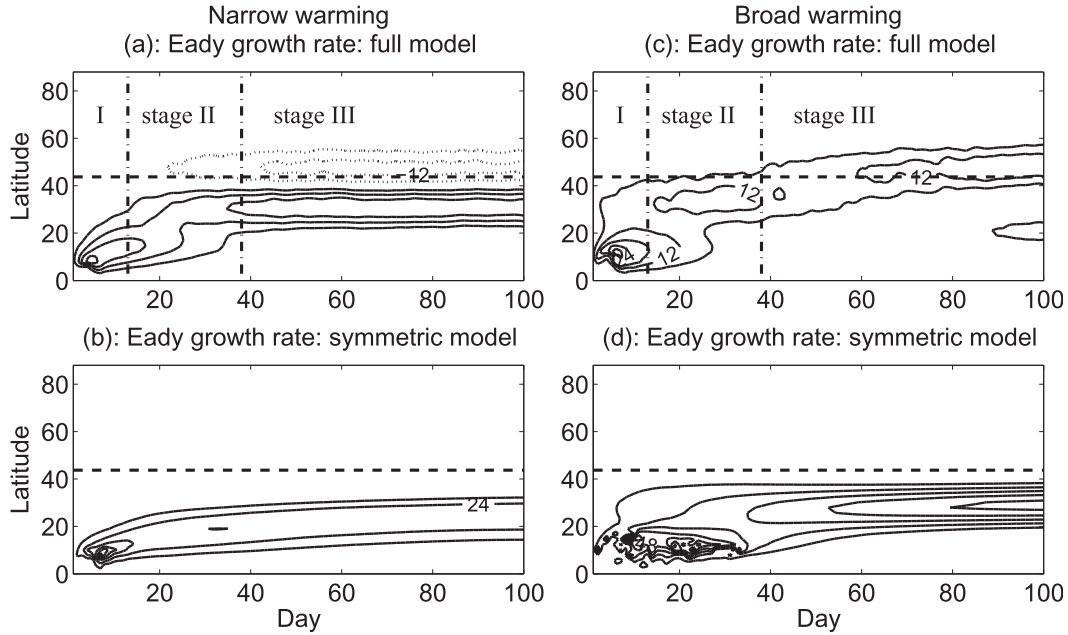
FIG. 8. The evolutions of low-level maximum Eady growth rate (MEGR) anomalies $(10^{-7} \, \text{s}^{-1})$ in the transient experiments of (a),(b) narrow and (c),(d) broad warmings. The MEGR adjustment in (a),(c) the full model and (b),(d) the zonally symmetric model. The MEGR anomalies are averaged vertically from 500 to 900 hPa. The black dashed line denotes the latitude of the climatological jet. The contour interval is $6.0 \times 10^{-7} \, \text{s}^{-1}$ in the full model and $1.2 \times 10^{-6} \, \text{s}^{-1}$ in the zonally symmetric model. The two dash-dotted lines in (a),(c) indicate day 13 and day 38, respectively.

c. Finite-amplitude wave activity diagnostics

We adopt a diagnostic framework developed by Nakamura and collaborators (Nakamura and Zhu 2010; Nakamura and Solomon 2010) by combining the conventional transformed Eulerian-mean (TEM) momentum equation with the finite-amplitude wave activity budget. Through relationship (8) the TEM momentum equation (6) is coupled with the pseudomomentum equation (e.g., Vallis 2006):

$$\frac{\partial A}{\partial t} + \overline{v'q'} = D, \tag{11}$$

where $A = (1/2)[(1/a)(\partial \overline{q}/\partial \phi)]^{-1}\overline{q'^2}$ is wave activity, which is negative of pseudomomentum, the second term is the Eulerian-mean eddy PV flux, and D represents the nonconservative processes, including the irreversible eddy mixing and diabatic term. Note that in the Eulerian formalism of the pseudomomentum equation, the cubic and higher-order terms in eddy amplitude have been neglected. Moreover, since the zonal mean PV gradient can change sign in the interior of the atmosphere and A becomes unrealistically large as the PV gradient approaches zero, the small-amplitude formulation has a rather limited applications for studying midlatitude eddy mean–flow interaction.

Recently, by taking a Lagrangian approach in estimating the wave activity and introducing equivalent latitude ϕ_e, Nakamura and collaborators (Nakamura and Zhu 2010; Nakamura and Solomon 2010) extended the concept of the wave activity to finite-amplitude waves and define finite-amplitude wave activity as

$$A(p, \phi_e) = \frac{1}{2\pi a \cos\phi_e}\left(\iint_{q>Q;\phi<\pi/2} q_{\text{qg}} \, dS \right.$$
$$\left. - \iint_{\phi_e<\phi<\pi/2} q_{\text{qg}} \, dS\right), \tag{12}$$

which measures the net displacement of the PV contours from zonal symmetry. The equivalent latitude for the PV value Q is determined by the requirement that the area enclosed by the PV contour toward the polar cap equals the area poleward of ϕ_e

$$\iint_{q>Q;\phi<\pi/2} dS = \iint_{\phi_e<\phi<\pi/2} dS = 2\pi a^2(1 - \sin\phi_e). \tag{13}$$

As such, there is a monotonic relationship between ϕ_e and Q for both hemispheres. More importantly, the

gradient of Q with respect to ϕ_e is always positive. We point out that A is nonnegative in the interior of the atmosphere and it assumes the familiar form of wave activity $\{A = (1/2)[(1/a)(\partial \overline{q}/\partial \phi)]^{-1}\overline{q'^2}\}$ for the small-amplitude limit.

It is shown in Nakamura and Zhu (2010) that with the wave activity defined as above Eq. (12), the non-acceleration theorem holds accurately for both small-amplitude and finite-amplitude eddies for inviscid, adiabatic fluid. Furthermore, within this hybrid Eulerian–Lagrangian framework, the eddy dissipation term can be further formulated as to be proportional to the Lagrangian PV gradient. Thus, Eq. (11) can be written as

$$\frac{\partial A}{\partial t} + \overline{v'q'} \approx -\frac{K_{\text{eff}}}{a}\frac{\partial Q}{\partial \phi_e} + \Delta\Sigma, \qquad (14)$$

where K_{eff} is the effective diffusivity of the irreversible mixing of PV across material surfaces (e.g., Nakamura 1996). In this paper, K_{eff} is calculated using the modified formalism for the hyperdiffusion used in our spectral dynamical core (see the appendix). Also, $\Delta\Sigma$ is the source of wave activity as a result of diabatic heating/cooling at equivalent latitude. It can be calculated by

$$\Delta\Sigma = \frac{1}{2\pi a \cos\phi_e}\left(\iint_{q>Q;\phi<\pi/2} \vartheta\, dS - \iint_{\phi_e<\phi<\pi/2} \vartheta\, dS\right), \qquad (15)$$

where $\vartheta = f(Q_r/\Theta_p)_p$ is the diabatic term in quasigeostrophic PV equation [e.g., Eq. (3.2.14) in Andrews et al. (1987)], $Q_r = (\theta_{\text{eq}} - \theta)/\tau$ is the diabatic heating/cooling resulting from relaxation, and θ_{eq} and θ are the radiative equilibrium potential temperature and potential temperature, respectively. The relaxation time is τ, the same as the value used at Held and Suarez (1994).

Making use of the relationship (8) under QG dynamics, we yield a budget equation for the E–P flux divergence:

$$\overline{v'q'} = \frac{1}{a\cos\phi}\nabla\cdot\mathbf{F} \approx -\frac{\partial A}{\partial t} - \frac{K_{\text{eff}}}{a}\frac{\partial Q}{\partial \phi_e} + \Delta\Sigma. \qquad (16)$$

Equation (16) states that the E–P flux divergence/convergence, which serves as a momentum source/sink for the zonal momentum equation (6), can be accounted for by the wave activity tendency, the irreversible wave dissipation and diabatic term. It is important to note that this is a hybrid framework, in which the E–P flux divergence is local in latitude, but the wave activity and PV gradient are evaluated following the material surface of the PV contours. The Eulerian and Lagrangian components of the diagnosis are aligned together by matching

the equivalent latitudes of A and Q and the latitude grids for $\overline{v'q'}$. Caution should be used in interpreting the budget within the deep tropics, where the QG approximations are no longer valid.

In view of the fact that the poleward transition of the eddy momentum forcing during stage II in the broad warming case cannot be accounted for by the lower-tropospheric baroclinicity, we now turn our attention to the upper-tropospheric wave dynamics, focusing on the effects of the irreversible wave processes. Figures 9a–d show the linear trends from day 13 to day 38 for the eddy PV flux, negative of the wave activity tendency, diabatic term, and irreversible wave dissipation. The change of the wave dissipation (Fig. 9d) shows similar pattern to the eddy PV flux (Fig. 9a). It seems that the diabatic term (Fig. 9c) also contributes to the eddy PV flux change, but its role is less important than the wave dissipation.

We further decompose the total dissipation into the component resulting from PV gradient change and that due to effective diffusivity change. We find that the reduction of the dissipation poleward of $40°$ and the associated eddy PV flux are mostly attributable to the decrease of PV gradient (Figs. 9e,g). The effective diffusivity increases in the same region where PV gradient decreases. This is consistent with the equation by Nakamura and Zhu (2010),

$$\frac{\partial}{\partial t}\left(\frac{1}{a}\frac{\partial Q}{\partial \phi_e}\right)$$
$$\approx \frac{1}{a^2}\frac{\partial}{\partial \phi_e}\left\{\frac{1}{\cos\phi_e}\frac{\partial}{\partial \phi_e}\left[\left(K_{\text{eff}}\frac{1}{a}\frac{\partial Q}{\partial \phi_e} - \Delta\Sigma\right)\cos\phi_e\right]\right\}. \qquad (17)$$

It states that if ignoring the thermal forcing $\Delta\Sigma$, the increase of the effective diffusivity aids in increasing the mixing and reduce the PV gradient. Besides, the effective diffusivity also increases in the area of $35°$–$40°$N around 300 hPa (Fig. 9h). The enhancement of the dissipation in such area (Fig. 9f) could partly explain the PV flux change in Fig. 9a. These suggest that the role of effective diffusivity is important in understanding the wave dissipation and eddy PV flux changes.

One may argue that it is the stirring that can enhance the effective diffusivity leading to a dissipation. While we agree that the large-scale stirring in an early stage can enhance the effective diffusivity that leads to dissipation later. It does not always lead a local dissipation change since the stirred waves can propagate away from the location of stirring, and in the simulations we also see frequent cancellations between instantaneous change of the PV flux and wave activity tendency. In the conservative limit with no change in dissipation and diabatic heating, the change in PV flux is expected to lead to fluctuations in the jet latitude, but not a shift in latitude
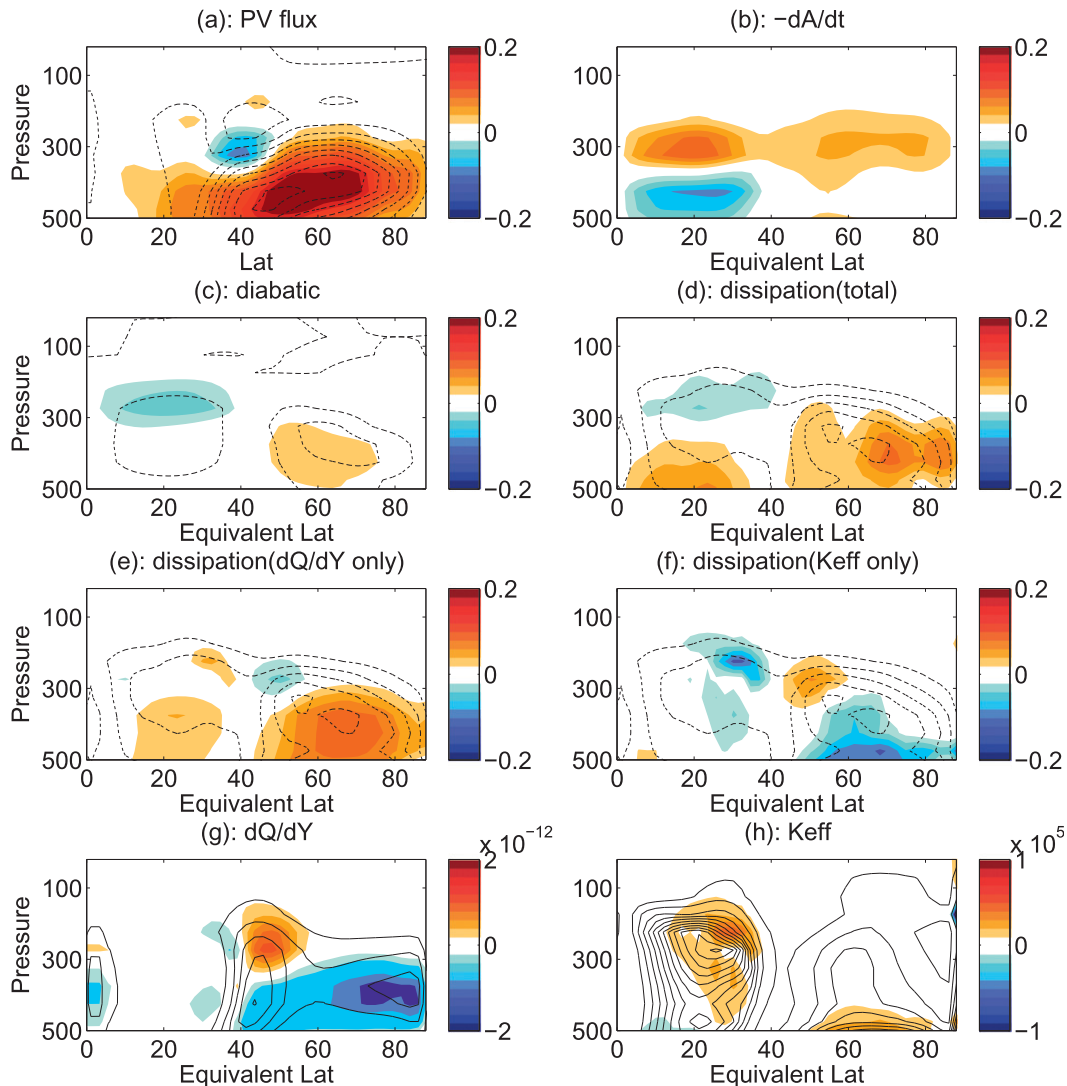
FIG. 9. The linear trends of the ensemble-mean wave activity budget [Eq. (16)] from day 13 to day 38 in the broad warming. (a) Eddy PV flux, (b) negative wave activity tendency, (c) total diabatic term change, (d) total dissipation change, (e) dissipation change resulting from PV gradient change, (f) dissipation change resulting from effective diffusivity change, (g) PV gradient change, and (h) effective diffusivity change. The contours in (a) are the climatological-mean PV flux. The contours in (c) are the climatological-mean diabatic term. The contours in (d)–(f) are the climatological-mean PV dissipation. The contour intervals in (a),(c)–(f) are $2 \, \mathrm{m \, s^{-1} \, day^{-1}}$. The contours in (g),(h) are climatological-mean $(1/a)(\partial Q/\partial \phi)$ (interval of $4 \times 10^{-11} \, \mathrm{m^{-1} \, s^{-1}}$) and K_{eff} (interval of $4.0 \times 10^5 \, \mathrm{m^2 \, s^{-1}}$). Note that all panels are shown above 500 hPa.

in the steady state. Here we argue that diffusivity can be regarded as a fundamental character of the circulation. For small-amplitude waves, the diffusivities are functions of the eddy displacements and are the same for different conservative tracers (e.g., Plumb 1979). Physically, the PV flux can be related to the parcel displacement about a Lagrangian PV gradient. Although a general discussion of eddy diffusivity is beyond the scope of this work, the parcel displacements are expected to be large and complex during a wave-breaking event.

6. Discussion and conclusions

In an attempt to address the different responses in the zonal mean circulation to the narrow El Niño–like forcing versus the broad global warming–like forcing, a sensitivity study is carried out with regard to the width, the vertical level, and the meridional gradient of the tropical heating using a dry atmospheric dynamical model. The results suggest that all of the previous studies can be reconciled within a single modeling system. With a tropical

heating comprising an equatorial heating and a subtropical cooling to increase tropical temperature gradient (TTG) (resembling the heating profile under El Niño conditions), this dry model produces a narrowed and strengthened overturning circulation and an equatorward shift of the eddy-driven jet, corroborating the pioneering work of Chang (1995). With the tropical upper-tropospheric warming (TUW), the model also replicates the robust poleward shift of the eddy-driven jet regardless the width of the heating, as found in Butler et al. (2010).

Additionally, in one set of experiments with the tropical warming imposed throughout the troposphere, the Hadley cell intensity increases for all widths of the heating, but the shift of the jet undergoes an equatorward-to-poleward transition as the meridional breadth of the heating gradually widens. The opposite shift in circulation for narrow versus broad warming in this set of experiments is analyzed in details. In keeping with previous studies (e.g., Brayshaw et al. 2008; Chen et al. 2010), we also find in the equilibrium response of our sensitivity experiments that the locations of the eddy-driven jet coincide with those of lower-level baroclinicity. However, this does not necessarily imply causality between the baroclinicity and the jet shift. The transition toward a poleward jet shift in the broad tropical tropospheric warming case provides a counterargument for the causality between the baroclinicity and eddy-driven wind. In the time sequences of the transient adjustment to the broad tropical heating, the lower-level baroclinicity actually increases first at the equatorward side of the jet and the eddy momentum acceleration at the poleward flank of the jet leads the poleward shift of the baroclinicity. Since the cause must occur before its effect in time, processes other than the change of baroclinicity must be responsible for initiating the jet shift.

The atmospheric response to the increased subtropical baroclinicity can be thought of as an ensemble mean of the changes in the baroclinic eddy life cycle (e.g., Simmons and Hoskins 1978; Hartmann and Zuercher 1998). In a typical baroclinic eddy life cycle, baroclinic eddies grow initially and reach a saturation in eddy amplitude, followed by nonlinear wave breaking and barotropic decay in eddy amplitude. When baroclinic eddies are decaying, the E–P flux vectors point downward in the extratropics (see Fig. 12 of Hartmann and Zuercher 1998). Throughout the life cycle, the surface temperature gradient is reduced as the result of the eddy-induced residual circulation. In comparison with our transient experiments, in the first stage (days 1–13), both the narrow and broad warmings are characterized by the enhanced lower-level baroclinicity in the subtropics as expected from diabatic heating. This is associated with the upward

wave burst (Figs. 7b,d), analogous to the baroclinic growth of eddies. In the second stage (days 13–38), the E–P cross sections in both the narrow and broad warmings are characteristic of barotropic decay in the extratropics, with the E–P vectors pointing downward.

We argue that a crucial difference between the narrow and broad warmings is the change of the surface baroclinicity at 20°–40°N during the second stage from day 13 to 38. For the broad warming, the lower-level baroclinicity in the subtropics ceases to increase, and the downward E–P vectors throughout the subtropics and extratropics are reminiscent of the barotropic decay. When baroclinic waves are decaying in an idealized eddy life cycle calculation, they are often accompanied by the equatorward wave propagation and poleward eddy momentum flux (LC1 in Fig. 12 of Hartmann and Zuercher 1998). By contrast, for the narrow warming, the lower-level baroclinicity in the subtropics (already present on day 13) continues to increase, in spite of the downward E–P vector in the extratropics. This provides additional source of lower-level wave activity in the subtropics.

Why does the subtropical lower-level baroclinicity cease to increase in the second stage for the broad warming but not for the narrow warming? In a typical baroclinic eddy life cycle, the lower-level baroclinicity is reduced by the eddy-driven residual circulation that induces cooling on the equatorward flank of the upper-level E–P flux convergence through the downward control mechanism. Although the E–P flux divergence patterns in the narrow and broad warmings are similar in the first stage, the magnitude is much greater in the broad warming case, which is more effective in reducing the subtropical baroclinicity. The tropical heating in the narrow warming run is also farther away from the midlatitude baroclinic zone, which helps shield the subtropical lower-level source of baroclinic waves from eddy mixing.

Generally speaking, in response to tropical diabatic heating, both the upper-tropospheric wave breaking and the lower-level baroclinicity are important in controlling the position of the jet stream and the terminus of the Hadley cell. The final destination of the eddy-driven jet can be thought of as the result of the tug of war between the wave dissipation in the upper troposphere and the change of baroclinicity in the lower troposphere. For the TUW experiments, in the absence of perturbation in lower-level baroclinicity, the upper-level wave breaking prevails, so that the westerly jet always shifts poleward, regardless of the latitudinal width of the heating. For the broad TTW experiments, in spite of the initial increase of the subtropical baroclinicity, it is dominated by the irreversible upper-tropospheric wave breaking during the poleward transition. For the narrow TTW and all of the TTG cases, however, the anomalous baroclinicity

gains a foothold at the equatorward side of the jet and dominates the final outcome of the competition.

APPENDIX

The Estimate of Effective Diffusivity

From the appendix of Nakamura and Zhu (2010), for the mth-order hyperdiffusion, the effective diffusivity can be directly diagnosed as

$$K_{\text{eff}} = \frac{\langle \kappa_{2m}(-1)^{m-1}\nabla[\nabla^{2(m-1)}q] \cdot \nabla q\rangle_Q}{[(1/a)(\partial Q/\partial \phi_e)]^2}, \quad (A1)$$

where $k_{2m} = 4.2 \times 10^{38}\,\text{m}^8\,\text{s}^{-1}$ is the diffusion coefficient for the eighth-order hyperdiffusion ($m = 4$) used in our spectral dynamical core. This diffusion coefficient damps the highest-order harmonic with an e-folding time of 0.1 day. Also, q is the QG PV, $\langle\cdot\rangle_Q$ denotes the area-weighted average around the Q contour, and ϕ_e is the equivalent latitude. For the regular diffusion $m = 1$, we obtain the conventional formulation of the effective diffusivity as in Nakamura (1996).

REFERENCES

Andrews, D. G., J. R. Holton, and C. B. Leovy, 1987: *Middle Atmosphere Dynamics*. Academic Press, 489 pp.

Brayshaw, D. J., B. J. Hoskins, and M. Blackburn, 2008: The storm-track response to idealized SST perturbations in an aqua-planet GCM. *J. Atmos. Sci.*, **65**, 2842–2860.

Bretherton, C. S., and A. H. Sobel, 2003: The Gill model and the weak temperature gradient approximation. *J. Atmos. Sci.*, **60**, 451–460.

Butler, A. H., D. W. J. Thompson, and R. Heikes, 2010: The steady-state atmospheric circulation response to climate change–like thermal forcings in a simple general circulation model. *J. Climate*, **23**, 3474–3496.

——, ——, and T. Birner, 2011: Isentropic slopes, downgradient eddy fluxes, and the extratropical atmospheric circulation response to tropical tropospheric heating. *J. Atmos. Sci.*, **68**, 2292–2305.

Chang, E. K. M., 1995: The influence of Hadley circulation intensity changes on extratropical climate in an idealized model. *J. Atmos. Sci.*, **52**, 2006–2024.

——, 1998: Poleward-propagating angular momentum perturbations induced by zonally symmetric heat sources in the tropics. *J. Atmos. Sci.*, **55**, 2229–2248.

Chen, G., and R. A. Plumb, 2009: Quantifying the eddy feedback and the persistence of the zonal index in an idealized atmospheric model. *J. Atmos. Sci.*, **66**, 3707–3720.

——, I. M. Held, and W. A. Robinson, 2007: Sensitivity of the latitude of the surface westerlies to surface friction. *J. Atmos. Sci.*, **64**, 2899–2915.

——, J. Lu, and D. M. W. Frierson, 2008: Phase speed spectra and the latitude of surface westerlies: Interannual variability and global warming trend. *J. Climate*, **21**, 5942–5959.

——, R. A. Plumb, and J. Lu, 2010: Sensitivities of zonal mean atmospheric circulation to SST warming in an aqua-planet model. *Geophys. Res. Lett.*, **37**, L12701, doi:10.1029/2010GL043473.

——, J. Lu, and L. Sun, 2013: Delineating the eddy–zonal flow interaction in the atmospheric circulation response to climate forcing: Uniform SST warming in an idealized aquaplanet model. *J. Atmos. Sci.*, in press.

Collins, M., and Coauthors, 2010: The impact of global warming on the tropical Pacific Ocean and El Niño. *Nat. Geosci.*, **3**, 391–397.

Edmon, H. J., B. J. Hoskins, and M. E. Mcintyre, 1980: Eliassen–Palm cross sections for the troposphere. *J. Atmos. Sci.*, **37**, 2600–2616.

Gong, T., S. B. Feldstein, and D. Luo, 2010: The impact of ENSO on wave breaking and southern annular mode events. *J. Atmos. Sci.*, **67**, 2854–2870.

Hartmann, D. L., and P. Zuercher, 1998: Response of baroclinic life cycles to barotropic shear. *J. Atmos. Sci.*, **55**, 297–313.

Held, I. M., and A. Y. Hou, 1980: Nonlinear axially symmetric circulations in a nearly inviscid atmosphere. *J. Atmos. Sci.*, **37**, 515–533.

——, and M. J. Suarez, 1994: A proposal for the intercomparison of the dynamical cores of atmospheric general circulation models. *Bull. Amer. Meteor. Soc.*, **75**, 1825–1830.

Hoskins, B. J., and D. J. Karoly, 1981: The steady linear response of a spherical atmosphere to thermal and orographic forcing. *J. Atmos. Sci.*, **38**, 1179–1196.

Kushner, P. J., and L. M. Polvani, 2004: Stratosphere–troposphere coupling in a relatively simple AGCM: The role of eddies. *J. Climate*, **17**, 629–639.

L'Heureux, M. L., and D. W. J. Thompson, 2006: Observed relationships between the El Niño–Southern Oscillation and the extratropical zonal-mean circulation. *J. Climate*, **19**, 276–287.

Lindzen, R. S., and B. Farrell, 1980: A simple approximate result for the maximum growth rate of baroclinic instabilities. *J. Atmos. Sci.*, **37**, 1648–1654.

Liu, Z., S. Vavrus, F. He, N. Wen, and Y. Zhong, 2005: Rethinking tropical ocean response to global warming: The enhanced equatorial warming. *J. Climate*, **18**, 4684–4700.

Lorenz, D. J., and E. T. DeWeaver, 2007: Tropopause height and zonal wind response to global warming in the IPCC scenario integrations. *J. Geophys. Res.*, **112**, D10119, doi:10.1029/2006JD008087.

Lu, J., and B. Zhao, 2012: The role of oceanic feedback in the climate response to doubling CO_2. *J. Climate*, **25**, 7544–7563.

——, G. A. Vecchi, and T. Reichler, 2007: Expansion of the Hadley cell under global warming. *Geophys. Res. Lett.*, **34**, L06805, doi:10.1029/2006GL028443.

——, G. Chen, and D. M. W. Frierson, 2008: Response of the zonal mean atmospheric circulation to El Niño versus global warming. *J. Climate*, **21**, 5835–5851.

Nakamura, N., 1996: Two-dimensional mixing, edge formation, and permeability diagnosed in an area coordinate. *J. Atmos. Sci.*, **53**, 1524–1537.

——, and A. Solomon, 2010: Finite-amplitude wave activity and mean flow adjustments in the atmospheric general circulation. Part I: Quasigeostrophic theory and analysis. *J. Atmos. Sci.,* **67,** 3967–3983.

——, and D. Zhu, 2010: Finite-amplitude wave activity and diffusive flux of potential vorticity in eddy–mean flow interaction. *J. Atmos. Sci.,* **67,** 2701–2716.

Orlanski, I., 2003: Bifurcation in eddy life cycles: Implications for storm track variability. *J. Atmos. Sci.,* **60,** 993–1023.

Plumb, R. A., 1979: Eddy fluxes of conserved quantities by small-amplitude waves. *J. Atmos. Sci.,* **36,** 1699–1704.

Robinson, W. A., 2000: A baroclinic mechanism for the eddy feedback on the zonal index. *J. Atmos. Sci.,* **57,** 415–422.

——, 2002: On the midlatitude thermal response to tropical warmth. *Geophys. Res. Lett.,* **29,** 1190.

Scinocca, J. F., and P. H. Haynes, 1998: Dynamical forcing of stratospheric planetary waves by tropospheric baroclinic eddies. *J. Atmos. Sci.,* **55,** 2361–2392.

Seager, R., N. Harnik, Y. Kushnir, W. A. Robinson, and J. Miller, 2003: Mechanisms of hemispherically symmetric climate variability. *J. Climate,* **16,** 2960–2978.

Simmons, A. J., and B. J. Hoskins, 1978: The life cycles of some nonlinear baroclinic waves. *J. Atmos. Sci.,* **35,** 414–432.

Son, S.-W., and S. Lee, 2005: The response of westerly jets to thermal driving in a primitive equation model. *J. Atmos. Sci.,* **62,** 3741–3757.

Vallis, G. K., 2006: *Atmospheric and Oceanic Fluid Dynamics: Fundamentals and Large-Scale Circulation.* Cambridge University Press, 745 pp.

Vecchi, G. A., A. Clement, and B. J. Soden, 2008: Examining the tropical Pacific's response to global warming. *Eos, Trans. Amer. Geophys. Union,* **89,** 81–83, doi:10.1029/2008EO090002.

Yin, J. H., 2005: A consistent poleward shift of the storm tracks in simulations of 21st century climate. *Geophys. Res. Lett.,* **32,** L18701, doi:10.1029/2005GL023684.